

Finding and minimizing systematic errors in dual-comb spectroscopy

M Walsh¹, P Guay¹, J D Deschênes², N Malarich³, I Coddington³, K Cossel³ and J Genest¹

¹ Centre d'Optique Photonique et Laser, Université Laval, Québec, Canada

² Octosig inc., Québec, Canada

³ National Institute of Standards and Technology, Boulder, Colorado, USA

Abstract. With sufficiently high signal-to-noise, several systematic errors become prominent in dual-comb interferometry measurements. This paper reviews several error sources including electrical, photo-detection, amplification and acquisition chain non-linearity. Sources of optical non-linearity such as self-phase modulation, cross-phase modulation and Raman soliton shifting are also covered, as are spectral fringing due to parasitic reflections and back-scattering. The non-linear response of the target sample itself can also be a source of errors. Methods to identify and minimize errors in experimental data are discussed. Good practices, instrument design strategies and tools, such as the dynamic range diagram, are suggested.

Submitted to: *J. Phys. B: At. Mol. Opt. Phys.*

Keywords: Frequency combs, dual combs, interferometry, spectroscopy, systematic errors

1. Introduction

Over the past decade dual-comb spectroscopy (DCS) has grown into a vibrant field of research. In part this is because the combination of broad-bandwidth, high spectral resolution, and high frequency accuracy possible with DCS allows for the exciting possibility of high precision in the identification and quantification of molecular

composition [1, 2]. As such the technique is steadily gaining adoption for laboratory as well as field-deployed spectroscopy applications [3, 4, 5, 6, 7, 8], which in turn continues to push the capabilities of DCS. As long-term coherent averaging of dual-comb interferograms has become broadly available [9, 10, 11, 12, 13, 14, 15], DCS measurements at very high signal-to-noise ratios (SNR) are being used to push the limits of measurement precision and accuracy and attention must turn to systematic errors that do not average out and will ultimately limit measurement performance. This review covers several sources of systematic errors in DCS, aiming to provide guidance on how to identify and minimize these errors in measurements.

DCS shares a great deal of commonality with classical Fourier transform spectroscopy (FTS), using the interference of two asynchronous optical frequency combs to replicate a scanning Michelson interferometer that exists at the core of an FTS instrument. In both systems a time-domain interferogram is measured and numerically transformed to get a spectrum. DCS can thus be seen as an evolution of Fourier transform spectroscopy [16, 17] and shares several of its advantages and noises sources. Similarities and differences between FTS and DCS are highlighted in this review where solutions developed over several decades for FTS can help understand some DCS problems.

Figure 1 shows two typical configurations for dual-comb experiments, highlighting key elements that will be discussed in the paper. In the top layout (a), the target sample is probed by both comb sources as it is located after the field combining coupler (or beam combiner). In the bottom (b) panel, the target sample is located before the coupler and is sensed by only one comb source. In the latter case, the gas impulse response is measured, and the molecular free induction decay (FID) is observed only on one side of the interferogram. In the former case, FID is measured on both sides of the interferogram center burst.

There are multiple distinct sources of systematic errors that will be addressed in this paper. Section 2 of this paper covers electrical sources of non-linearity. Detection using a single photo-diode or a balanced pair, electrical amplification and analog to digital conversion can all have a non-linear response and introduce errors. Section 3 next discusses how non-linear optical processes can introduce bias in DCS measurements. Non-linear field propagation in optical fibers, before and after the coupler or the target sample affect measurement errors differently. Self and cross phase modulations (SPM and XPM) notably act differently on the dual-comb interferogram when happening before or after the coupler. Spectral broadening

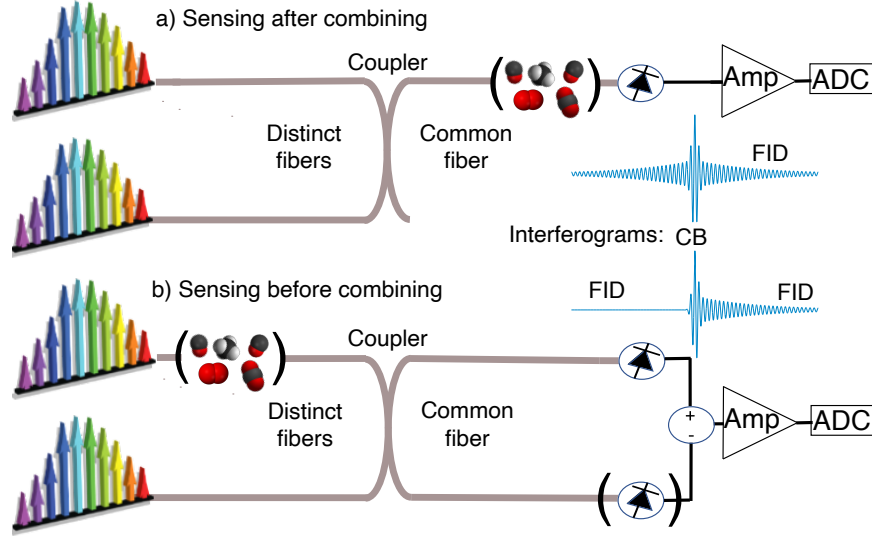


Figure 1. Two Typical DCS configurations showing several key elements that will be referenced in later discussions. The target sample can be probed either by one (a) or the two (b) comb sources when located respectively before or after the beam combining coupler. Detection can use a single photo-diode or two in a balanced scheme. Each geometry can have slightly different implications for controlling systematic errors. “Amp” denotes electrical amplification, CB is the interferogram center burst around the zero path difference, FID is for the molecular free induction decay and ADC stands for Analog to Digital Converter.

processes used to expand spectral coverage can reduce the field coherence and be prone to noise amplification. Raman soliton shifting, for instance, comes with the risk of introducing extra noise, bias, or altogether removing the ability of performing dual comb interferometry. Another source of optical non-linearity can come from the response of the studied sample itself. This can be interpreted as meaningful information, or as an error source if only the linear response is compared against spectroscopic databases. Asymmetric Fano profiles have been observed in that context. Section 4 finally provides an overview of how parasitic optical reflections and back scattering add spurious signals and alter measurements.

Phase noise between the two combs can also cause bias [18]. It is however assumed here that the dual-comb sources are sufficiently mutually stable [19] and that phase noise as well as sampling jitter are properly managed either through source stabilization [20, 21], interferogram correction [9, 22] or both [15].

Beyond spectroscopy, dual-comb interferometry is also used for ranging [23, 24, 25, 26], tomography [27, 28, 29] and for the synchronization of remote optical clocks [30]. Several systematic errors discussed here in a spectroscopy context also affect these and must be considered for time-domain dual-comb applications.

Fighting systematic errors is a never-ending battle, where successive order of magnitude improvements are increasingly harder to gain. Current limits are therefore mentioned and quantified, with hints of potential avenues for further improvements.

1.1. The fundamental DCS hypothesis

Before delving into specific topics, it is convenient to remind the reader of a fundamental DCS hypothesis: DCS relies on the assumption that one measures the cross-correlation between the two optical fields. This is achieved by varying the time delay between successive repeating patterns of the two fields. For mode-locked laser sources emitting short pulses, this implies that all pulse pairs must be identical, up to a known relative inter-pulse delay and phase. This often overlooked hypothesis is necessary for the measured interferograms to be a proper estimator for the optical field cross-correlation. Any deviation from this hypothesis, such as varying pulse shapes, will lead to distortions in the cross-correlation and, likely, systematic errors in the recorded spectra. As with most systematic errors these distortions will not improve with additional averaging.

2. Electrical non-linearity and dynamic range

Non-linearity of the photo-detection, amplification and digitization elements of the signal acquisition chain can introduce non-linear distortions in measured interferograms. To first order, this often manifests as a saturation that can be viewed as an intensity dependent gain applied to the ideal linear interferogram, as illustrated in fig. 2. In this picture, the non-linearity is assumed to be static: only the unperturbed linear interferogram value at a given time is needed to compute the non-linear interferogram at the same instant. Detector and electronic non-linearity and its mitigation have been extensively studied for FTS [31, 32, 33] and several solutions can be applied to DCS. Higher peak intensities and larger detection bandwidths however mean that non-linearity can't always be assumed static in DCS. Additionally, temporally spreading the power in the interferogram by applying a large differential

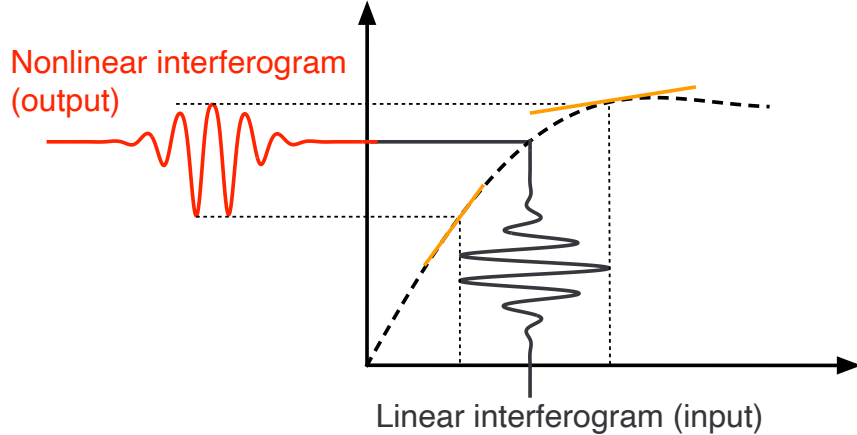


Figure 2. Non linearity in the detection and acquisition chain can to first order be modeled as a static signal dependent gain (the slope of the dashed line). In the illustration here, the gain is smaller at large than at small signal amplitude.

chirp to the combs is more practical in DCS and offers a new means to manage electrical non-linearity.

Due to electrical saturation, most dual-comb measurements are carried out using sub-mW optical power levels when tens of mW are usually available from the lasers' outputs [1]. Avoiding saturation can thus limit the signal-to-noise ratio for a given measurement duration. Very often, electrical amplification is the first offender. Photo-diodes can also be non-linear but can support much higher optical powers before distorting the signal. Finally, digitizers can exhibit their own subtle form of non-linearity that can counter-intuitively impact weak signals such as a free-induction decay tail while faithfully preserving the large variations at the center of an interferogram. This section covers the understanding, observation and mitigation of detector, electrical chain and acquisition card non-linearity. In section 2.5 a useful visual tool, the dynamic range diagram, is also introduced to help identify the limiting component and optimize signal acquisition chains.

2.1. Amplification chain non-linearity

It is common in DCS to use commercial detectors with a built-in trans-impedance amplifying stage. At the high required bandwidths (100 MHz or more), these detectors often have a fixed gain, are usually designed for other applications such

as optical coherence tomography, and are not extensively tested with short, high-intensity pulses. The saying that $100 \mu\text{W}$ of comb power is sufficient to saturate a detector [1] is largely due to the fact that these detectors usually have too much gain for DCS and are not designed to handle a GHz-bandwidth short current pulse at the amplifier's input.

Figure 3 (left) shows the impulse response of a Thorlabs PDA10CF[‡] detector (trans-impedance gain 2000 V/A , total gain 8000 with internal second stage) measured with a femtosecond mode-locked laser having a $f_R = 16.9 \text{ MHz}$ repetition rate. This ensures the detector response is significantly shorter than the repetition rate, and that pulses are temporally separated enough so that successive responses do not overlap. Impulse responses are acquired using a high speed oscilloscope having significantly (4 GHz) more bandwidth than the photo-detector. The impulse responses are normalized by the incident average power. Since a linear impulse response is expected to scale with power while maintaining a constant shape, this normalization highlights any non-linear behavior. In this paper, all impulse response measurements report the measured average powers given the specified laser repetition rate. To help converting to average power at different repetitions rates, the pulse energy is also provided.

It is seen on fig. 3 (left) that the impulse response largely preserves its shape and seems to behave linearly up to pulses energies of 3 pJ . Starting at 6 pJ , the shape change is however obvious, with the broader response and slower ringing implying that the detector's bandwidth is reduced at higher powers. This is confirmed on the transfer functions shown in fig. 3 (right). This is a very common behaviour. As pulse energy increases, the photo-diode and amplifier electrical bandwidth reduces. One must thus ensure the detector has the proper bandwidth for all measured power levels. Since the interferogram is a modulated signal, one wants to avoid a situation where fringe troughs are not measured with the same transfer function as fringe crests. That would imply dynamic non-linearity depending upon frequency content.

It can also be observed on fig.3 (left) that impulse responses have significant content past 10 ns even if the electrical bandwidth is quoted and observed to be 125 MHz , at least at low power. This means that when such a detector is used with a higher repetition rate dual comb source, the impulse response triggered by a pulse pair is not zero at the arrival of the next one. Tick marks in fig 3 (left) are chosen to help visualize the impulse response overlap for common repetition rates of 100 MHz (10 ns) and 200 MHz (5 ns).

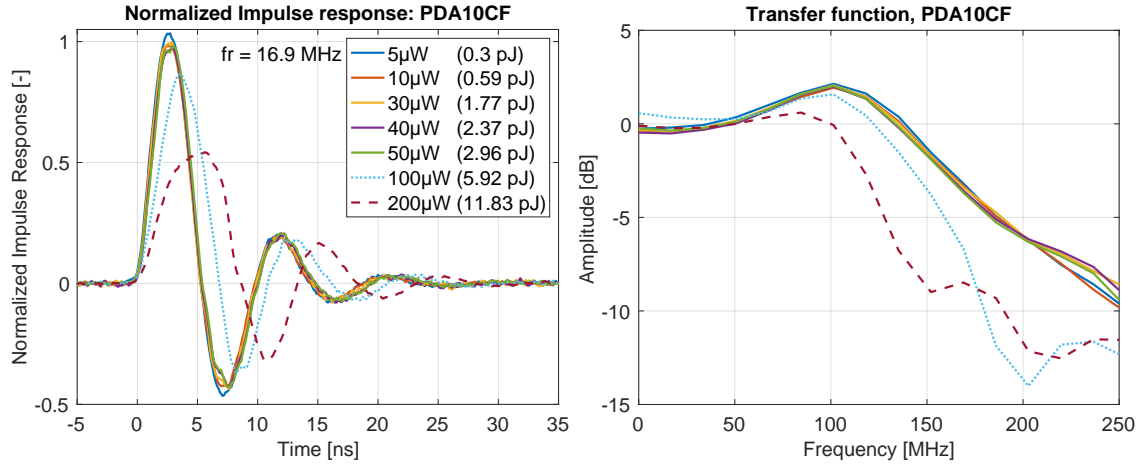


Figure 3. (Left) Impulse response of a Thorlabs PDA10CF[‡] detector, normalized by the measured incident input power. This shows that the detector impulse response does not solely scale in amplitude when the power is increased. (Right) Transfer function obtained from the Fourier transform of the impulse responses. Average powers are given for a mode locked laser having a 16.9 MHz repetition rate.

This temporal overlap is not problematic as long as the impulse response doesn't change shape and scales linearly with power. The detector can then be modeled as a linear time invariant filter that convolves the input photo current with its constant impulse response. In the spectral domain, this corresponds to the application of a time independent transfer function.

When the impulse response's shape changes with power, a measured pulse pair will however experience varying contributions from previous pulses depending on their intensity, creating hysteresis and thus dynamic non-linearity. It is therefore important to ensure either that the detector impulse response does not change shape significantly, or that its influence is reduced to zero over time scales shorter than the inter-pulse delay.

It shall be noted that errors can occur before changes in the impulse response shape are obvious. For instance, fig. 3 (left) seems to suggest that the detector is linear up to 3 pJ, which amounts to 600 μW of average power for a 200 MHz repetition rate. In high precision applications percent level changes on the detector response can be significant. For the specific detector example used here, concentrations errors

up to 1% can be observed for detected powers as small as only a few hundred of μW of detected power [34].

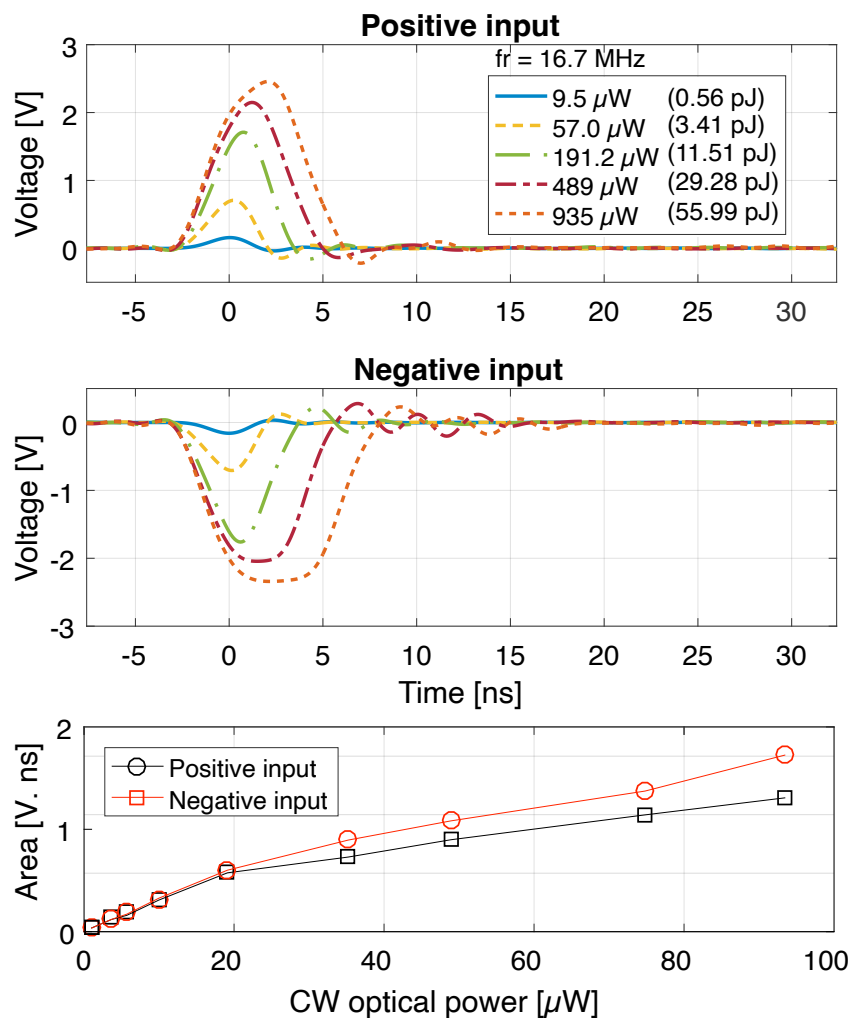


Figure 4. Impulses responses for the positive (top) and negative (middle) inputs of a Thorlabs PDB130[‡] amplified balanced detector do not change in the same manner with increasing power. Impulse response amplitude as well as area (bottom) is not scaling linearly with power and its slope is not the same for positive and negative inputs. Average powers are given for a mode locked laser having a 16.7 MHz repetition rate.

The problem is similar for amplified balanced detectors. Figure 4 shows the

impulse responses for the positive (top) and negative (middle) inputs of a Thorlabs PDC130C[‡] detector having a total gain of 25000 V/A. It is seen that the shape changes are radically different for both inputs.

In DCS it is common to electrically filter the detected signal with a low pass filter at half the repetition rate to avoid Nyquist sampling issues. Such a properly designed filter effectively integrates the pulse response over the filter time constant making the measurement primarily sensitive to the pulse area. In this case, estimating the area of each individually resolved pulse with a linear time invariant low pass filter may produce linear interferometry measurements even if the detector response is not linear, as will be seen in section 2.2.

For the PDC130C[‡], the impulse responses areas (fig. 4 (bottom)) also do not scale linearly. This means that even when individual pulses can be time-resolved, the interferogram amplitude will suffer from static non-linearity. The divergence between the positive and negative input slopes also mean the detector is properly balanced only for low powers, defeating the non-linearity mitigation arising from balanced detection [35].

The non-linearity observed in fig. 3 and 4 is consistent with saturation of the Texas Instrument[‡] OPA-847 operational amplifier used in both the PDA10 and PDB130 detectors and whose recovery from negative saturation is more oscillatory than from positive saturation ([36], page 7). It was also confirmed experimentally that saturation for the PDB130C arises in the amplifying stages, after the photocurrents are subtracted. This was done by comparing the results of sending signals sequentially and simultaneously to both inputs.

2.2. Photo-detector non-linearity

With amplified detectors providing excessive gain and saturating, it makes sense to evaluate how non-amplified detectors perform when the trans-impedance element is a passive resistor. Figure 5 displays the impulse responses for the positive (top) and negative (middle) inputs of a Thorlabs BDX[‡] balanced photo-diode pair whose difference current is sent to a 50 Ω resistor.

The positive and negative impulse responses change shape, meaning that the photo-diode pair response behaves non-linearly. The exponential shape having a slower decay as power increases is typical of excess carriers creating a screening electric field slowing the carriers and reducing the detector bandwidth [37, 38].

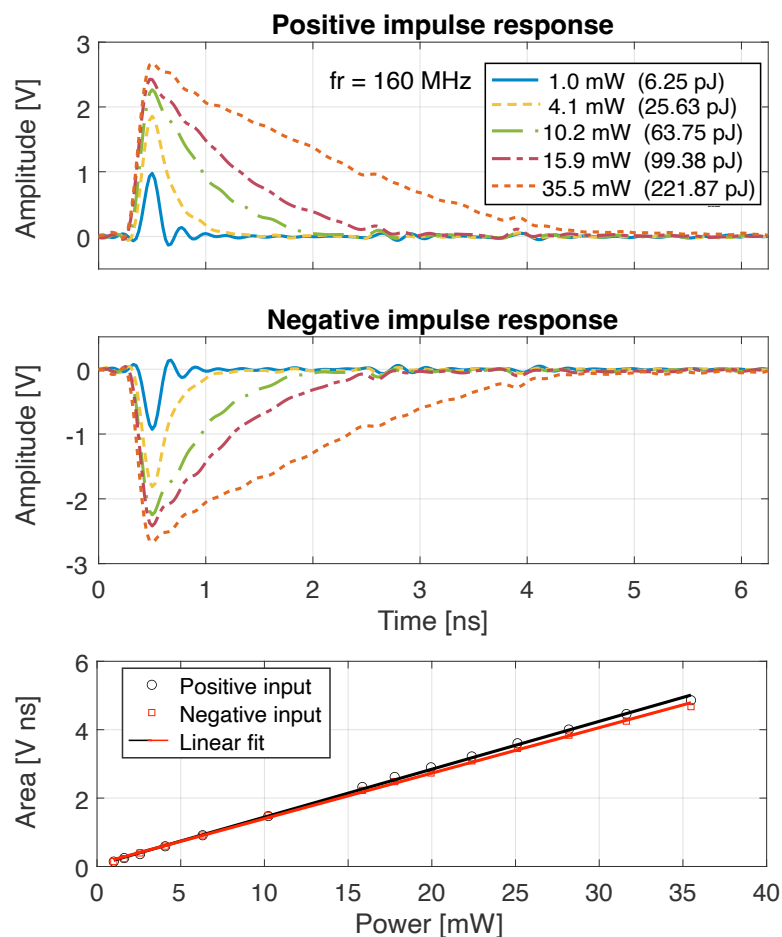


Figure 5. Impulses responses for the positive (top) and negative (middle) inputs of a Thorlab's BDX[‡] detector. Both impulse responses change, but in a very symmetric manner. The shape is typical of charge carrier slowing down due electric field screening. Impulse responses do not overlap even for a 5 ns period and the areas are very linear with power. Linear comb interferometry can be performed with repetitions rates up to 200 MHz and pulse energies up to 220 pJ, even if the detector response is non linear. Average power is for a 160 MHz repetition rate

The positive and negative impulse response shapes are however remarkably similar, so that balancing is expected to be maintained along a wide power range. The impulses responses also decay to zero before 5 ns for pulse energies as high as 200 pJ and their areas (fig. 5 (bottom)) are highly linear for average powers from 0

to over 30 mW. There is thus no impulse response overlap for repetition rates as high as $f_r = 200$ MHz and the value of each point of the interferogram low pass filtered in a $f_r/2$ bandwidth, which is proportional to the area, will therefore be linear. Linear DCS can thus be performed with this detector with high repetition rate sources and for high incident power, even if the detector response is non linear [39].

2.3. Non-linear spectral artifacts: checking for non-linearity

The transformation between a linear and non-linear interferogram (IGM) shown in fig. 2 can, under the static non-linearity hypothesis, be written as a polynomial expansion [31, 33]:

$$IGM_{NL}(t) = a_0 + a_1 IGM_L(t) + a_2 IGM_L^2(t) + a_3 IGM_L^3(t) + \dots, (1)$$

where IGM_{NL} and IGM_L are respectively the non-linear and linear interferograms and where a_0, a_1, a_2, \dots are the expansion constant coefficients. This means that the measured non-linear spectrum (SPC) can be expressed as a function of the linear spectrum:

$$SPC_{NL}(f) = a_0 \delta(f) + a_1 SPC_L(f) + a_2 SPC_L(f) * SPC_L(f) + a_3 SPC_L(f) * SPC_L(f) * SPC_L(f) + \dots, (2)$$

where $*$ denotes the convolution, $SPC_i(f)$ is the Fourier transform of the interferogram $IGM_i(t)$ and the Dirac function $\delta(f)$ is often ignored because the signal is AC coupled.

Terms containing self-convolutions of the linear spectrum ($SPC_L(f) * SPC_L(f) * \dots$) yield spectral artifacts at harmonics of the linear signal [31, 40]. Figure 6 shows a linear (black) and non-linear (red) DCS measurement along with a cartoon representation of the spectral artifacts. For a model linear interferogram having a boxcar shaped spectrum (dashed blue), the second order non-linear term manifests as a triangular artifact at twice the signal frequency as well as around DC (two-dashed yellow) and the third order convolution creates a smoother artifact at the third harmonic, but also has contributions in a frequency band around the fundamental frequency (dash-dotted green). Convergence of the series expansion ensures coefficients decrease for higher order terms. Self-convolutions also spread errors on wider spectral ranges. Higher order non-linear spectral artifacts usually decrease in amplitude to the point terms beyond the third order are difficult to observe and are negligible, as long as the system is not driven deep into non-linearity.

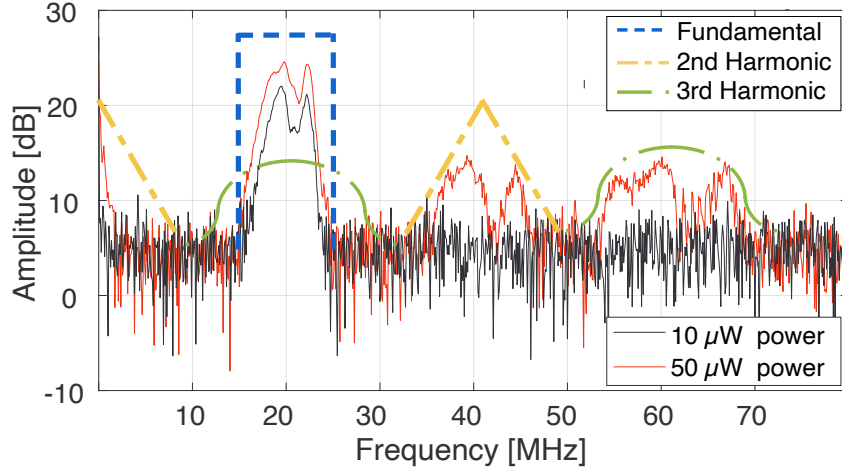


Figure 6. DCS measurements in the presence of static non-linearity which creates spectral artifacts at integer multiples of the fundamental frequency. The relative amplitude of these artifacts can be used to evaluate the magnitude of systematic errors introduced by non-linearity. A low power non-linearity free spectrum is shown in black. A spectrum with non-linearity onset is shown in red. Dashed cartoon representations show a boxcar (blue) linear spectrum producing triangular (yellow) second order artifacts through self-convolution and even smoother third order artifacts (green).

The linear signal is affected by a gain a_1 but also distorted by all artifacts that might spectrally overlap with the fundamental frequency band of interest. All odd-order non-linear terms create an artifact at the fundamental frequency. Even-order terms can also overlap with the fundamental signal depending upon its width and the choice of repetition rate difference between the two combs.

The amplitude of the spectral artifacts allows an estimation of the error on the fundamental signal. These artifacts are mostly created by the large peak-to-peak signal at the interferogram center burst and are a measure of the gain change over the signal total dynamic range. Seeing spectral artifacts 10 dB below the main signal, as in the extreme case shown in fig. 6, implies that the gain changes by up to 10% on the full interferogram amplitude range.

The impact of this can be profound. In spectroscopy applications for example, the molecular free induction decay (FID) information is a small signal at the wings of the interferogram and experiences an unperturbed small signal gain within the

bounds of the total possible range. Concentration errors arising from the difference between the large signal gain at the center burst and the small signal gain on the FID can thus be as high as the relative spectral artifact amplitude.

Monitoring those artifacts therefore provides a convenient way to check for, minimize and quantify non-linearity in a DCS setup. Because the electrical signal at the fundamental frequency, but also all non-linear artifacts, broaden when the repetition rate difference is increased, artifacts often overlap so they are not easily observable. When checking for non-linearity in a detection chain, it is thus a good practice to set a small enough repetition rate difference such that second and third order spectral artifacts are not spectrally overlapped with the main signal, as in fig. 6. To maintain non-linearity induced systematic errors below 0.1%, spectral artifacts need to be smaller than 30 dB ($10 \log_{10}()$, optical power ratio) below the fundamental signal. Observing them on the high resolution Fourier-transform of single-shot interferograms can thus be difficult.

Complicating matters further is the fact that non-linearity cannot be characterized after averaging if the phase changes between successive interferograms. Assuming a phase difference ϕ between successive linear interferograms, the n -th harmonic artifacts will have a $n\phi$ phase difference. Phase correction of the detected signal before averaging brings contributions at the fundamental frequency in phase, but not higher harmonic terms. The visible spectral artifacts at n times the fundamental frequency are thus reduced by averaging, but not the non-linearity contributions in the fundamental frequency band (i.e the artifact at $1-f$ created by 3rd order non-linearity does not average out).

The solution is to perform a short Fourier transform of unaveraged interferograms over a small window around the center bursts. This apodization will strongly suppress noise contributions and can be done in real time on a digitizer or an oscilloscope to provide quick feedback on the non-linearity in the setup.

2.4. Acquisition card non-linearity

At the end of any DCS acquisition chain sits an analog-to-digital converter (ADC), which exhibits a very different form of non-linearity. Real ADCs do not exhibit a perfect staircase conversion from analog voltages to digital levels. In practice they can be very linear for large signals but their imperfections can lead to gain distortions for very small signals. ADC distortion is often characterized by plotting

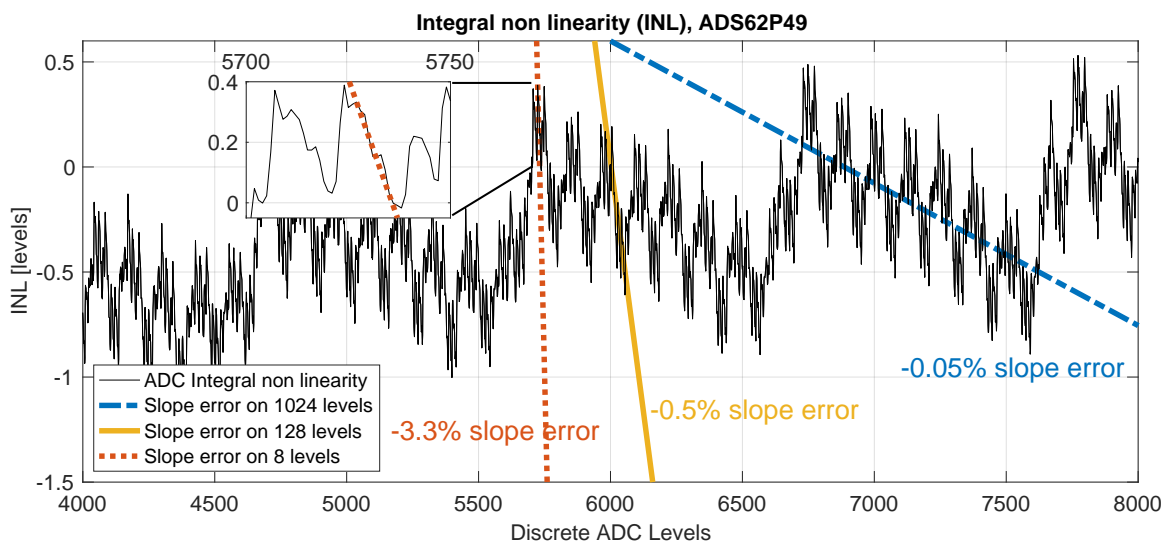


Figure 7. Integral non linearity (INL) of an ADS62P49 ADC. A slope on the INL curve is a deviation from the full ADC range gain.

the difference, in number of levels, between the ideal voltage-to-level relation and what is achieved by an imperfect ADC over its entire range. This quantity is called the ADC's integral non-linearity (INL). Figure 7 shows such an INL curve for a 14 bits Texas Instruments[‡] ADS62P49 ADC on an Abaco[‡] FMC108 board. Like most ADCs used in DCS it has a pipeline architecture with successive stages having slightly imperfectly different gains leading to nested INL saw-tooth structures. In the case shown here, periods of $2^3 = 8$ levels, $2^7 = 128$ levels and $2^{10} = 1024$ levels are seen in fig. 7 .

Because INL is expressed relative to the ideal ADC relation, any non-zero slope indicates a deviation from the full range conversion gain. For this specific ADC, as shown in fig. 7, small signals that span only 8 levels can experience a gain deviating by up to 3.3% compared to the large signal gain. Signals spanning 128 and 1024 levels can respectively be subject to gain errors of 0.5% and 0.05%.

In spectroscopy the effect of ADC non-linearity is similar to detector and amplifier non-linearity in that the small molecular FID signal is not subject to the same gain as the large interferogram center burst, leading to potential concentration errors. The difference is here is that the small signal is experiencing intensity dependent gain rather than the large center burst, meaning that non-linear spectral

artifacts would be very difficult if not impossible to observe by looking for harmonics. Fortunately the effects are possible to reliably model if the INL curve is measured [41] and can typically be mitigated in the acquisition system.

Proper use of an ADC usually involves making sure random noise sources at the converter input are larger than the deterministic conversion pattern. To first order this means that the noise floor must match the device equivalent number of bits (ENOB) [42]. In the example here, the ADS62P49 ENOB is 11.3 bits so, according to the manufacturer, the input random noise should cover more than 2.7 bit levels of the 14 bit ADC. This is somewhat consistent with suppressing the 8 level pattern that yields a 3.3% slope error on signals smaller than 8 levels, but the wider structure on 128 levels may still cause 0.5% gain errors. For measurements requiring very high gain accuracy it may be necessary to go beyond ENOB and measure the ADC INL to determine the required noise amplitude.

In DCS measurements, the random noise source is ideally dominated by the photon shot noise, but could also be due to the thermal noise introduced by the trans-impedance amplifier or the laser relative intensity noise. One can, in principle, adjust the amplification before the acquisition card to bring the random noise level comfortably above the ADC structured noise. For high dynamic range signals common in DCS, this approach is constrained by the maximal signal amplitude set by the ADC full scale range.

The well-known solution to ADC non-linearity is dithering [43, 44, 45]. Rather than amplifying to ensure sufficient noise, a small signal is added at the ADC input. This additive rather than multiplicative approach prevents the maximal signal amplitude from scaling and thus has a smaller dynamic range cost. The most straightforward dither signal to add is white noise, with a level adjusted according to the ADC ENOB and INL. This however inevitably decreases the measurement signal to noise ratio regardless of where the signal is located in frequency.

A noisy dithering signal with frequency content outside the signal bandwidth presents as an interesting alternative [41]. For instance, if the DCS signal is always constrained to be above 10 MHz, a band-limited noise source around 1 MHz, whose total noise variance is adjusted to span the desired number of levels seems very appealing. It must however be remembered that this small dithering signal will experience the staircase (+INL) ADC conversion, which is a non-linear mapping with very high frequency content. Several harmonics of the dithering signal will be generated in this process. This non-linearity further happens before the sampling

operation. The dithering signal harmonic series will thus be aliased around multiples of the sampling frequency (f_s). With band-limited noise, this usually generates a white frequency noise floor at a level lower than the band limited noise power spectral density. One must make sure this noise floor is smaller than other noise sources to avoid degrading the in-band signal to noise ratio. This may be straightforward for dithers utilizing a moderate fraction of the Nyquist bandwidth but may be an issue if the dither bandwidth must be tightly constrained to avoid interference with the DCS signal.

A solution that avoids generating dithering noise content at all frequencies is to change the DC value between each acquired interferogram. This way, when several interferograms are averaged, the small signal gain is also averaged over a properly chosen number of ADC levels, converging to the large signal gain. Only the discrete spectrum point at zero frequency is then affected. In the example of fig. 7, varying the DC by 1000 levels ensures less than 0.05% error between the large signal and average small signal gains while using only $1000/8192 = 12\%$ of the total ADC range.

Several ADCs are however AC-coupled such that adding an adjustable DC is not possible. In such cases, a tone at the sampling frequency f_s can be used [43, 44]. By virtue of the sampling theorem, this tone as well as all its harmonics alias to zero frequency, again affecting a single point in the measured discrete spectrum. Adjusting the amplitude of this tone thus produces the same result on the sampled interferogram than changing the DC level. In a similar manner, an adjustable tone at $f_s/2$ can be used. This affects only two points in the spectrum (0 and $f_s/2$).

2.5. Designing an acquisition chain: the dynamic range diagram

The knowledge and constraints from the preceding sections can be used to help design optimal acquisition chains for specific DCS applications. This is more easily achieved using a visual tool clearly showing the limits of each link. The tool effectively tracks the maximal and minimal signal values at each step and is hence appropriately called a *dynamic range diagram*.

Figure 8 shows such a simplified diagram for a DCS measurement in the near infrared. Each step of the acquisition chain is illustrated with a colored vertical band. The signal and noise levels are followed across each step with blue (signal) and red (noise) lines respectively. The design aim is to best adapt the received optical power and noise level to the acquisition card dynamic range, while respecting the

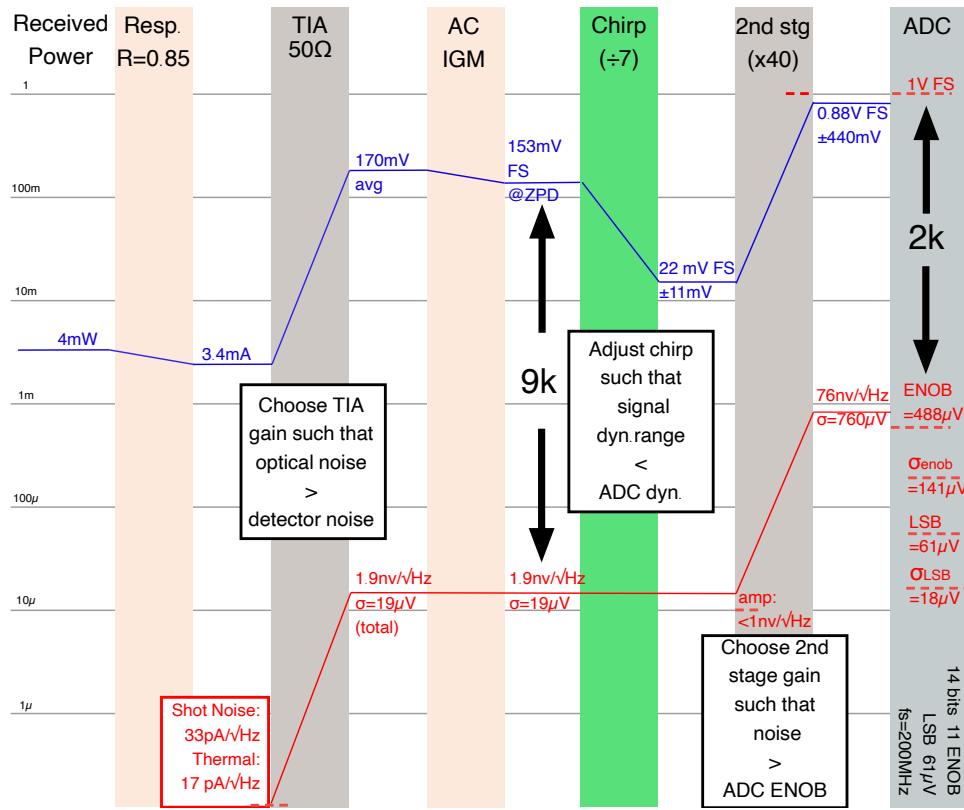


Figure 8. Dynamic range diagram for a DCS tracking signal and noise levels at each stage of the detection chain (shown as vertical columns). Here we consider a case where 4 mW of total average comb power is available and a 1 V full scale (FS) 14 bits data acquisition card having an 11 equivalent number of bits (ENOB) sampling at 200 MHz. Design decision points and shown in black boxes. The AC coupling step converts average power to the interferogram full scale range, taking into account modulation efficiency. “Resp” stands for the photo-detector responsivity, “TIA” for trans-impedance gain, “ZPD” for zero path difference. Note that the “Chirp” stage is typically applied to one of the frequency combs well before the detection stage but is shown after detection since it impacts the peak voltage and not the optical power.

constraints at each step. In doing so, the dynamic range diagram provides a visual representation of the most stringent limitations and thus of where optimisation efforts must be devoted.

The diagram in fig. 8 begins with the received power. Here, it is assumed that 4 mW is available at the photodetector. For an open-path experiment the diagram might start with the launched power and include a link-loss step. Variable return power levels can also be tracked simultaneously on the diagram.

The detector responsivity (Resp. $R = 0.85$ A/W) converts the detected power in the photocurrent at the trans-impedance amplifier input. At this step, the expected shot noise power spectral density (PSD) is computed from the average photo-current. If the measurement is expected to be limited by laser relative intensity noise (RIN), this noise term can also be computed and tracked on the diagram. Here, it is assumed that the measurement is shot noise limited, with a $33\text{pA}/\sqrt{\text{Hz}}$ PSD. The measurement bandwidth is set by the Nyquist limit ($f_s/2$) of the ADC sampling at $f_s = 200$ MHz in this example.

2.5.1. Choice of trans-impedance gain

Knowing the optical signal and noise levels, the required trans-impedance gain can be computed. The design goal here is to choose the trans-impedance resistor such that its thermal noise is under the fundamental optical noise sources. With the photocurrent thermal and shot noise PSDs being respectively $4k_bT/R_{TIA}$ and $2qI_{av}$, the trans-impedance resistor is chosen as:

$$R_{TIA} > \frac{2k_bT}{qI_{av}}, \quad (3)$$

where k_b is Boltzman's constant, T is the temperature, q is the electron charge and I_{av} is the average photocurrent. At room temperature, eq. 3 yields $R_{TIA} > 50 \Omega$ for $I_{av} \approx 1$ mA and $R_{TIA} > 1000 \Omega$ for $I_{av} \approx 50 \mu\text{A}$.

This means that for photo-currents larger than 1 mA a passive 50Ω resistor that is conveniently impedance matched to the subsequent RF chain is generally sufficient, provided that the photo-diode capacitance is sufficiently low to achieve the required bandwidth when in parallel with the 50Ω resistor, as it is the case for the BDX detector described in section 2.2. For powers between $50 \mu\text{W}$ and 1 mW, a trans-impedance gain of $1\text{k}\Omega$ suffices. While choosing higher trans-impedance gains reduces the thermal noise contribution relative to optical noise sources, this also puts unneeded constraints on the active trans-impedance amplifier that is likely

required to achieve the > 100 MHz bandwidth. Larger than needed trans-impedance gain usually implies less bandwidth and more distortion induced by the active components.

In the example of fig. 8, it is assumed the measurement is shot noise limited and the noise PSD is computed to be $1.7 \text{ nV}/\sqrt{\text{Hz}}$ (1.9 total with thermal noise) across the $50 \text{ } \Omega$ resistor. The 3.4 mA signal photocurrent yields a voltage of 170 mV . The noise standard deviation ($\sigma = 19 \text{ } \mu\text{V}$) is computed in the 100 MHz bandwidth fixed by the ADC Nyquist range.

Interferograms are usually AC-coupled, most often even before the trans-impedance stage. The AC coupling step in fig. 8 also includes the modulation efficiency of the interferometer ($\eta = 90\%$ here) to compute a maximum signal amplitude of 153 mV at the center burst (or ZPD for zero optical path difference).

At this point, the DCS dynamic range problem is apparent. The ratio between the maximal signal amplitude and the noise standard deviation is $153/0.017 \text{ mV} = 9000$, as indicated by the thick black arrows. This is significantly larger than the dynamic range of $2^{11} = 2048$ for a typical 14 bits (11 bits ENOB) ADC. Choosing a $\times 40$ gain for the second amplifying stage ensures the $\sigma = 19 \times 40 = 760 \text{ } \mu\text{V}$ noise standard deviation is larger than the $488 \text{ } \mu\text{V}$ ENOB level of the ADC. This however brings the maximal 153 mV signal level to 6.12 V which is way above the 1 V ADC full scale. Simply said, the signal has a too large dynamic range to fit in the ADC bottleneck. One can't accommodate simultaneously the largest and smallest signal levels. A 9000 dynamic range would require an ENOB of $\text{Log}_2(9000) = 13.2$ bits, which is currently not available for $> 100 \text{ MHz}$ sampling frequencies.

2.5.2. The need for chirp

One powerful tool for combating detection chain non-linearity is the application of differential optical chirp to the comb sources to chirp the interferogram. Putting a dispersive element in one of the interferometer arms can be seen as having a different zero path delay (ZPD) location for each signal frequency. Chirp thus spreads the interferogram center burst over a longer duration and commensurately reduces its maximal amplitude. A parabolic phase reshuffles a stationary white noise without changing its time-domain statistics. In DCS, chirping the interferogram can thus be used to reduce the signal dynamic range and compensate for the lack of ADC dynamic range.

This idea of chirping the interferogram to reduce dynamic range has been

proposed several times in FTS [46], where it unfortunately does not work. This is because in FTS the path difference is achieved using a spatial displacement. Geometrical effects, notably beam divergence, badly affect the instrument line shape when a dispersive medium is placed in a single interferometer arm [47], because dispersion affects differently optical rays at various angles in the instrument. Such an FTS configuration is also often called “field-widened” [48].

In DCS, the delay is created in the time domain such that no varying differential spatial beam propagation occurs between the two interferometer arms. This is why DCS does not have an instrument line shape caused by geometrical considerations. Even for free space DCS, wavefront curvatures are not changing with optical path delay. It follows that DCS interferograms can be chirped without affecting the instrument spectral resolution [49].

In the fig. 8 example, interferogram chirp is chosen to reduce the maximal amplitude by a factor 7, bringing the maximal fringe amplitude to ± 11 mV and the signal dynamic range to 1300, fitting comfortably within the 2000 ADC dynamic range.

In the near infrared, chirping is easily achieved by inserting an additional fiber length at one of the two lasers outputs. The exact length needed to achieve a certain amplitude reduction ratio depends upon the fiber dispersion curve as well as on the spectrum width and center frequency but usually, less than 10 meters is sufficient. The exact location of the chirping fiber in the setup also depends upon minimisation of optical non-linearity [50, 51] (see section 3) but differential chirp can only be applied before the combs are combined. Chirping fiber should also in general be placed before picking up the optical referencing signals to make sure phase drifts occurring in this fiber are accounted for [49].

In the near infrared, chirping is best realised with non bi-refrangent fiber. While using polarization maintaining fiber is possible, a typical polarisation extinction ratio of 20 dB means that 1% of the light is travelling in the other polarisation axis. Polarisation mode dispersion then creates a time-retarded copy of the field producing etalons and spectral fringing in a manner similar to parasitic reflections (see section 4), but that are extremely difficult to manage.

For DCS in other spectral regions, such as the mid-infrared, chirping can be more difficult. In systems with optical frequency conversion, chirping can’t be done before the non-linear crystals to maintain optimal conversion efficiency. After conversion, the beams are usually free-space and low loss fiber is most of the time not available. If

chirp is mandatory for dynamic range considerations, it must then be introduced with grating pairs. In cases where chirped pulse amplification is performed, compression after the high-power amplifiers can be adjusted to keep a residual differential chirp between the two DCS arms.

2.5.3. Choice of second stage gain

Once the signal and ADC dynamic ranges are adjusted, either by chirp or by choosing an ADC with a sufficient ENOB, the gain of the second amplifying stage is selected (if needed) to best adjust the minimal and maximal signal levels going in the ADC. Here, with the factor of 7 gained from chirping, the $\times 40$ amplitude gain brings the shot noise standard deviation to $\sigma = 760 \mu\text{V}$, above the $488 \mu\text{V}$ ADC ENOB. The maximal signal is then at 880 mV full scale, 3000 levels below the card 1 V full range. The second stage is also chosen such that extra added noise, specified by its noise figure, is smaller than fundamental (shot or thermal) noise contributions.

If, at the ADC input, the random noise is smaller than the range over which INL is significant, a dithering signal is added. Here $760 \mu\text{V}$ corresponds to 12 levels of the 14 bits ADC, and it is known from fig. 7 that dithering is needed over at least 100 levels. A dithering tone at $f_s = 200 \text{ MHz}$ that slowly changes the average interferogram value (after aliasing) by a few hundred levels (15 mV) is thus needed.

2.6. Correcting for residual non-linearity

Optimizing the design of the acquisition chain should minimise non-linearity. There is however no guarantee that non-linearity can be totally eliminated in all cases. If non-linear spectral artifacts are still observed one can, after ensuring that this non-linearity can be assumed static, use software corrections based on the minimisation of out of band spectral artifacts [33, 40]. Care should however be taken in performing this correction before interferogram averaging if the phase of successive center bursts is not constant.

3. Optical systematic error sources

Optical non-linearity can modify the dual-comb field in a manner that violates the fundamental DCS hypothesis. Depending upon the cause, this may increase random noise, systematic errors or altogether make DCS measurements impossible. Self-

phase modulation (SPM) and cross-phase modulation (XPM) as well as Raman soliton self-frequency shifting are discussed in this section. The probed sample or scene may itself respond non-linearly and this can either be viewed as useful information or as a source of systematic errors.

3.1. Pulse interaction

Improperly controlled coherent optical non-linearity can lead to errors. For instance, in a commonly used dual-comb spectroscopy scheme, the two comb sources are combined in a common fiber before sensing the sample of interest. In fig. 1 this corresponds to case a), with pulse pairs propagating in a common fiber between the coupler and the sample. Such a scheme of combining the fields as soon as possible minimizes relative phase fluctuations and jitter as well as allows distributing the dual-comb beat note to one or several remote experiments, such as for field-deployed open-path spectroscopy [5]. Pulses having moderate energies (< 50 pJ) traveling in a common weakly non-linear media such as single mode fiber (SMF) over as little as 10 m have however been shown to create percent-level spectral transmittance errors [51]. Spectral residuals with a very characteristic systematic error shape, seen in fig. 9 have been observed with different setups and for several molecules, including CO, CO₂, H₂O and CH₄.

Non-linear optical propagation leads to very counter-intuitive impacts on DCS. Non-linear transformations at the optical field level imply that changing the order of optical elements in the setup changes the measurement results. Having separate non-linear propagation in distinct fibers before the coupler (or beam splitter) or propagation in common fiber before or after the sensed sample (such as a molecular ro-vibrational response) all lead to different outcomes.

In a two-beam interferometer, the interference condition is established where beams are combined. If the two fields are in phase at the coupler inputs, most of the optical signal will be directed to one of the outputs yielding an interferogram crest at this output. If the fields are 180° out of phase, signal goes to the second output and a fringe trough is observed at the first output.

Let's now suppose that an optical fiber having a non zero third order non-linear coefficient $\chi^{(3)}$ is connected to the coupler output. It is important to note here that $\chi^{(3)}$ processes are power conserving [52]. Notwithstanding linear losses and ignoring the target sample for the moment, this means that placing a detector directly at one

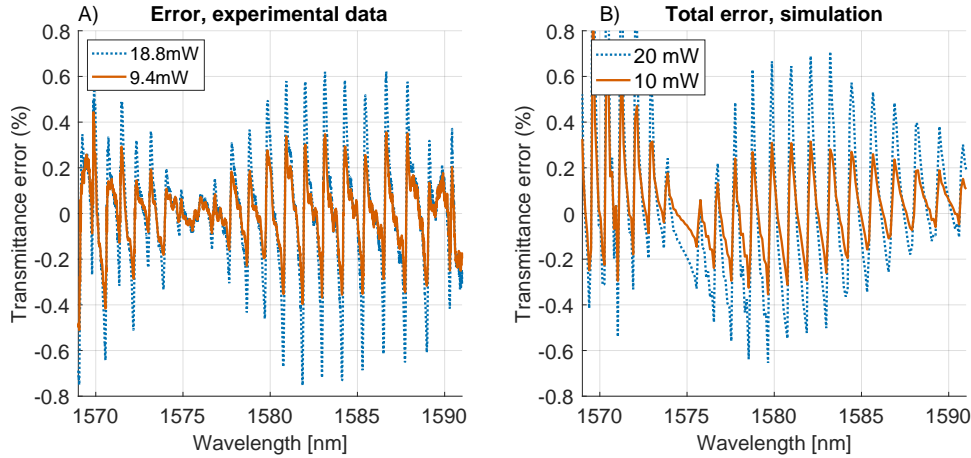


Figure 9. Self and cross phase modulation create systematic errors when pulses from the two comb sources propagate in a common non-linear fiber. Here the XPM-induced characteristic asymmetric shape having a width matching the line spacing (not the line width) is observed in CO experimental data (left) and simulations using the non-linear Schrödinger equation.

of the coupler outputs, or after a length of non-linear fiber will lead to exactly the same detected intensity for all pulse pairs and thus the same interferogram. This has been extensively verified by numerical simulations of the non-linear Schrodinger equation and experimentally validated [51].

The actual optical field is however changing upon propagation in the non-linear fiber. The power-conserving non-linear process reduces the spectral amplitude at certain optical frequencies while adding content at others. For moderate powers, where the soliton order is smaller than one, this is dominated by SPM.

The optical field exciting the target sample is thus not the same as the field for which the interference condition was established at the coupler. The measured interferogram after the target sample is therefore not the field cross-correlation filtered by the sample's response. Its the cross-correlation of the fields at the coupler plus the molecular response to a different field.

At first order, this SPM-induced effect appears in spectroscopy as a line depth error and is thus a concentration error. A line around a given frequency is excited by more (or less) field amplitude than what can be deduced from the interferogram Fourier-transform. Otherwise said, the spectral baseline is from the field cross-

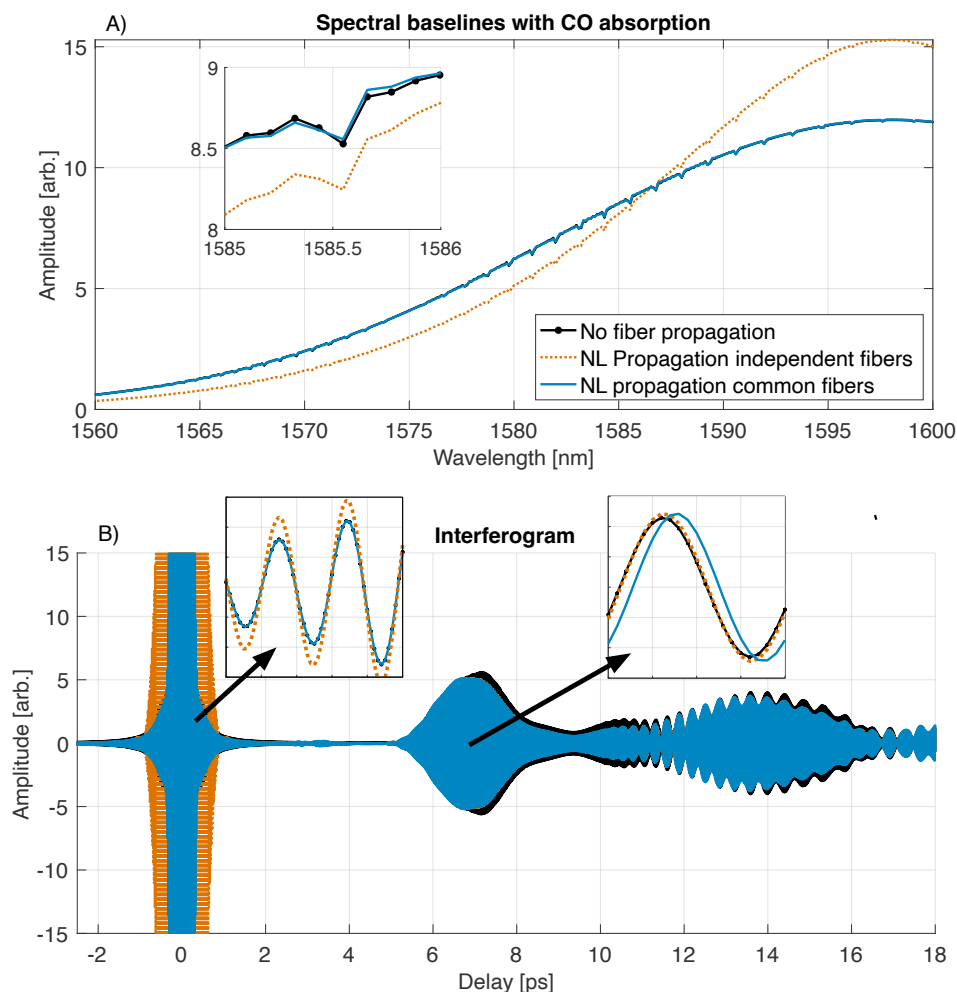


Figure 10. Simulated spectra (A) and interferograms (B) obtained when non linearity occurring in standard optical fiber is taken into account. Self-phase modulation changes the field spectral content, but not the total power. Changes in the spectral baseline are seen for the case of nonlinear propagation of the two combs in independent fibers (red), but the measured spectrum does not reflect this change if the power-conserving non-linearity occurs in a common fiber, after the overlap of the two fields in the coupler (blue curve matches the black one corresponding to no fiber propagation). Cross-phase modulation induces an unaccounted delay, best seen in the second insert of panel (B), where the common fiber propagation leads to a phase error for the molecular FID feature.

correlation at the coupler while the line depth is from the field at the sample.

If SPM occurs in distinct fibers before the coupler, then the field interference at the coupler reflects the modified fields. A target sample right after the coupler is then excited by a field with the same spectral content. The interferogram reflects the modified spectral content and the sample response to it. No systematic error is then observed on line depths.

This is seen in figure 10 where the overall spectrum shape change is seen when non-linear propagation occurs in distinct fibers for the two combs (dashed red curve) while non-linearity in a common fiber after the coupler produces a spectral baseline and interferogram center burst (blue) closely matching the spectrum obtained when there is no nonlinear fiber propagation (dotted black).

When the two fields propagate in the same non-linear fiber, cross-phase modulation also acts on the pulses. It has been shown [53, 54, 51] that XPM creates an attractive (for normal group velocity dispersion) or repulsive (for anomalous group velocity dispersion) interaction. In the DCS context, this means the inter-pulse delay in a pair exciting the sensed sample is not what one expects. This attractive interaction pulls interferogram points closer to the zero path difference and hence introduces sampling errors [55]. This is seen in fig. 10 (B) and its right side insert where the interferogram arising from non-linear propagation (blue) in a common fiber shows a clear contraction and phase error. This attractive force reduces in magnitude with greater inter-pulse delays and must go to zero at the zero path difference. The sampling error is thus greater for intermediate delays and mostly affect the first few recurrences of the molecular free induction decay. This explains why errors are related to the line spacing. Since this is a delay error on the sampling grid, the error is proportional to the interferogram derivative [55]. This elucidates why the observed and simulated errors in fig. 9 are asymmetric.

SPM effects can be reduced by having less common fiber propagation or potentially by using hollow core fibers with low non-linearity. SPM effects can also be reduced by pre-chirping the optical pulses from both lasers before going into the common fiber, usually ~ 10 m of standard fiber suffices. This is in addition to any differential chirp between the two arms to manage dynamic range issues (see section 2.5.2). Pre-chirping does not however reduce the impact of the sampling error due to XPM. Chirped pulses then interact more weakly, but for a longer duration. Errors are smaller at lower delays in the interferogram, but this is traded for errors at higher delays. The asymmetric error shape becomes sharper. The error is however not

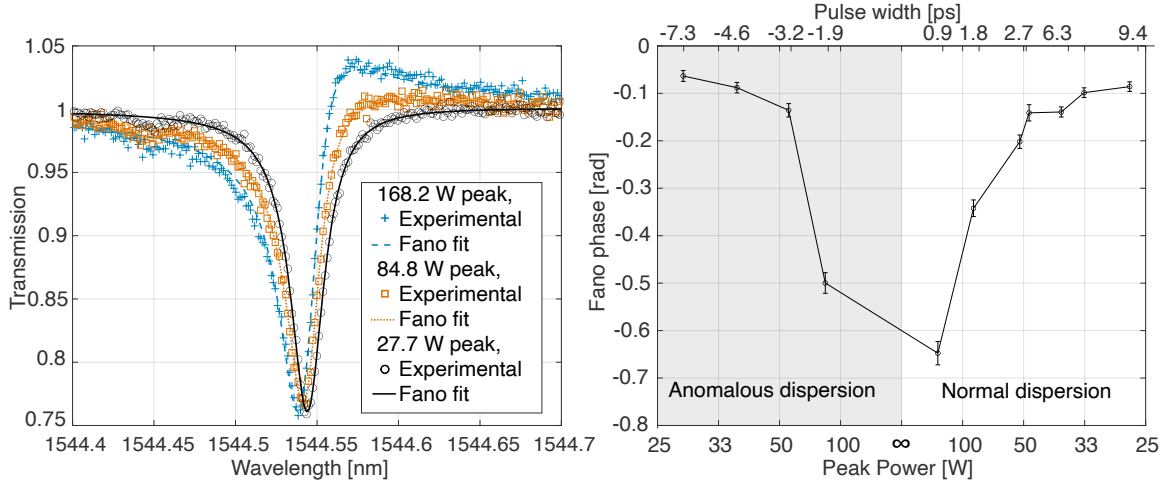


Figure 11. High peak intensities yield distorted line shapes following a Voigt-Fano profile. Here a 16.5 cm cell containing 5.3 kPa (40 Torr) of H₁₂CN is probed by 30 mW from a single comb having a 160 MHz repetition rate. Chirping fiber is used before the cell to vary the pulse duration and peak power. (Left) Distorted line shapes for three peak powers. (Right) Fano phase as a function of peak power and pulse duration.

significantly reduced in amplitude before pre-chirping lengths present other practical problems, such as loss (> 100 m). Note that while we focus here on propagation in a common fiber near the end of the setup, these effects could also appear in dual-comb systems where the pulses share a common laser cavity as the pulses co-propagate in a non-linear medium, at a higher intra-cavity power and over several round trips.

3.2. Non-linear response of the spectroscopic sample: Fano line shapes

To avoid systematic errors due to common fiber propagation, the sample can be placed before the optical coupler, at the left most location in fig. 1. This also makes measurements sensitive to the amplitude and phase of the target sample [20]. With all systematic error sources discussed in this paper minimized, it is found that measured absorption line shapes depend upon the peak field intensity, as shown in fig. 11. This has been observed with different setups for several molecules, including HCN, C₂H₂, H₂O and CO₂ [50].

For the dataset presented in fig. 11, 30 mW of power from a single comb is used

to probe a 16.5 cm, 5.3 kPa (40 Torr) H¹²CN gas cell (Wavelength References[‡]). Various lengths of dispersive fibers are used to chirp pulses before the target sample. This adjusts the pulse length and the peak power in the gas cell. The left panel shows how the HCN line at 1544.55 nm goes from following a Voigt profile for a 26.7 W peak power probing the cell to asymmetric profiles for 84.8 and 168.2 W.

For all cases, the observed asymmetry fits well with a Voigt-Fano profile. The Fano $F_c(\nu)$ profile is most simply expressed as a rotation of the complex Lorentz line shape $L_c(\nu)$. A Fano phase ϕ_F [56] is applied: $F_c(\nu) = L_c(\nu)e^{j\phi_F}$. In the time domain, this implies that the molecular free induction decay is phase shifted by ϕ_F .

The total observed profiles also have a Gaussian component. Without the Fano phase, the complex Voigt line shape is obtained via convolution between the complex Lorentzian and Gaussian contributions $V_c(\nu) = L_c(\nu) * G(\nu)$. Taking the Fano phase into account, the measured profile is [57]:

$$C_c(\nu) = F_c(\nu) * G(\nu) = L_c(\nu)e^{j\phi_F} * G(\nu) = V_c(\nu)e^{j\phi_F}, \quad (4)$$

showing that the Voigt-Fano profile $C_c(\nu)$ is simply a rotation of the complex Voigt line shape. Upon application of the Beer-Lambert Law, the measured complex line is $e^{-C_c(\nu)}$ where the complex rotation brings part of the dispersive line shape to the absorption profile.

The right panel of figure 11 shows the Fano phase found when fitting Voigt-Fano profiles to lines measured while varying the pulse chirp and hence duration (top axis) and peak power (bottom axis). A separate measurement with ten times less power revealed negligible Fano phase for all pulse durations, hinting that reducing the peak power is the key factor here.

Any mechanism shifting the free induction decay phase can introduce Fano-like line distortions. This can arise from a coupling between the discrete level and an absorption continuum, which was the case originally studied by Ugo Fano [58]. The phase shift can also emanate from perturbations coming from another weakly coupled oscillator, such as in line-mixing [59, 60]. It can also be induced using a strong field laser to momentarily Stark shift the transition [56]. In doing so, a line shape can be switched from a Fano to a Lorentz profile and vice-versa.

Understanding the exact mechanism shifting the FID phase in molecular spectroscopy with sub picosecond pulses and moderate (< 1 kW) peak powers could enable using this effect to extract physical information on the probed molecule. In the meantime, chirping before the target sample is a solution to minimize this systematic

error source. For very high precision applications, up to 40 m of chirping fiber is necessary to reduce the Fano phase below 0.08 rad [61]. Increasing the size of the probing beam to reduce the power density can be an alternative to avoid dealing with long chirping fibers.

3.3. Non-coherent spectral broadening

Any incoherent optical non-linear effect that insufficiently preserves the optical field amplitude and phase from one pulse to another quickly reduces DCS quality, introducing extra random noise, bias or altogether destroying the dual-comb interference, depending upon the severity of the coherence loss. This might for example come from relative intensity noise amplification and varying non-linear phase shift in intensity dependent non-linear effects.

One example that can produce negative results for DCS is using Raman soliton self-shifting. This approach seems more attractive than supercontinuum generation to efficiently generate power in a specific spectral range away from the frequency combs' native spectra. Figure 12 however shows the added phase and intensity noise on the dual-comb beat note. This extra noise scales with the wavelength shift. In the case presented here, it effectively prevents any useful measurement at 1960 nm.

For this dataset, two Menlo Systems C-fiber[‡] mode-locked lasers with a native spectrum around 1560 nm, are independently Raman shifted to 1960 nm. This is a commercially purchasable option from Menlo. For fig. 12, the repetition rate difference between the two combs is set as small as possible (20 Hz) and a very short portion of the dual-comb interferogram at the maximum of a center burst fringe is displayed. Given the 250 MHz repetition rate, there are 2500 pulse pairs in the shown 15 μ s time span.

Panel A) in fig. 12 shows that the interferogram amplitude and phase are very smooth for light in the comb native spectral range around 1560 nm. The amplitude is following the fringe evolution while the detrended phase is showing a ± 50 mrad excursion from electrical noise at 200 kHz, most likely from a switching power supply. The displayed amplitude and phase noise for the 1560 nm interferogram is filtered in 10 MHz (dashed black curve) to show signal quality in the bandwidth normally occupied by the dual comb signal in this experiment. It is also shown in a 90 MHz bandwidth to provide a fair comparison with the 1960 nm case that exhibits wide band noise.

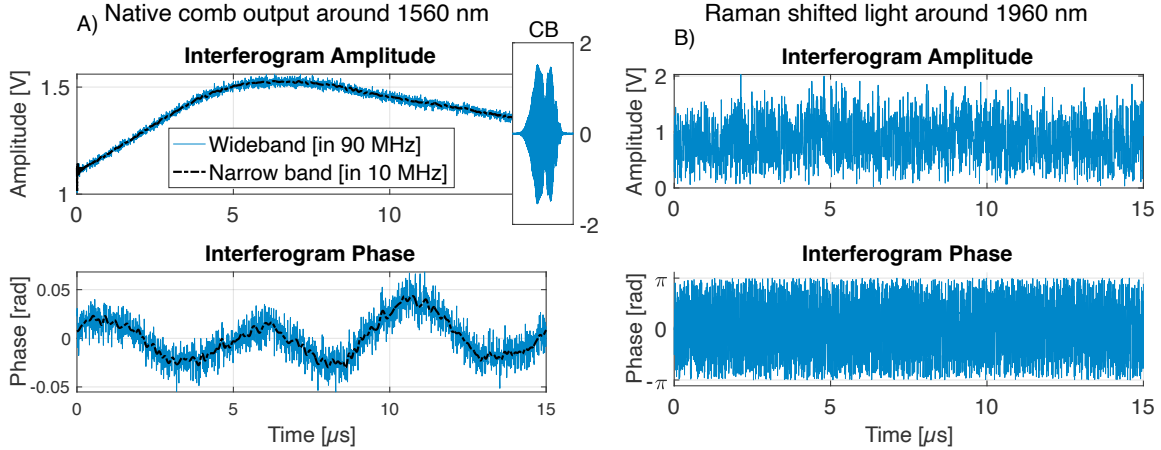


Figure 12. Small portion of a fringe at center burst for a dual-comb beat note between two c-fiber Menlo lasers[†]. (A) The interferogram for the native comb outputs at 1560 nm shows smooth amplitude and phase in the 10 MHz bandwidth that could normally be used for DCS measurements (dashed black). The insert shows the full center burst (CB) fringe amplitude (B) The Raman shifted outputs around 1960 nm produce an interferogram having wide band intensity and phase noises, over the full comb Nyquist range (0 to $f_r/2 = 125$ MHz). Noise is filtered in a 90 MHz bandwidth to remove technical noise sources near 0 Hz and $f_r/2$.

Panel B) shows on the other hand that the interferogram obtained when beating the two Raman-shifted outputs around 1960 nm has a totally random phase that can be anywhere on a $]-\pi, \pi]$ interval from one pulse pair to another. The interferogram amplitude is accordingly anywhere on the fringe for each pulse pair.

This data is for all practical purposes unusable for DCS. Tracking the interferogram phase at 1960 nm on a pulse to pulse basis would likely not be sufficient to retrieve a proper interferogram on a correct delay grid. The dual comb beat note phase is set by the fields' carrier frequencies. Such a drastic interferogram phase noise means the carrier frequencies are changing significantly one relative to another. It thus does not matter that Raman-shifted light have been shown to exhibit comb-like features with modes at discrete frequencies defined by the repetition rate of the pumping field [62, 63]. Changes in the carrier frequency while having discrete spectral modes means the power distribution between the modes is changing. A changing spectrum implies a changing pulse envelope and thus a violation of the DCS hypothesis. For this system, it was also validated with a free-space interferometer

having a path delay of exactly one pulse that the inter-pulse phase noise for each of the Raman shifted sources is larger than 1 radian, with severe intensity noise.

For smaller shifts, the added phase and intensity noise will be smaller and DCS might be possible, albeit with a degraded SNR. One must however also pay attention to potentially added biases, as these noisy non-linearities might not act in a similar manner on the large interferogram centerburst and on the small FID signal, especially if there is common propagation in non-linear media.

4. Etalons and optical back-scattering

Parasitic reflections in the setup create time-delayed copies of the optical signal. This in turn creates delayed copies of the interferogram, as shown in figure 13. These parasitic signals are often called etalons because they arise from the presence of an unwanted Fabry-Perot etalon in the optical path. In the spectral domain, these interferogram echos add a sinusoidal spurious component often labeled spectral fringing, or channeled spectrum in FTS.

For laboratory spectroscopy, when a reference measurement without the gas is used to calibrate the gas spectrum and obtain the spectral transmittance, etalons cancel out as long as they are stable between the gas and reference measurements. In practice, this is not the case for all parasitic reflections, as minute drifts in component lengths displace the spurious signals in delay such that calibrated measurements are then worse, containing two parasitic copies rather than one.

In FTS, great care is thus taken to eliminate etalons caused by parasitic reflections. All critical surfaces have anti-reflection coatings and all substrates are wedged so that any parasitic reflection propagates at an angle from the main beam. The wedge angle is usually chosen such that parasitic light is away from the field of view, or at least tilted enough such that the interferometric modulation efficiency with the main beam is almost zero. Minimizing etalons is however rarely considered as it should when designing a dual-comb instrument. In particular micro-optic fiber components and splices between dissimilar fiber types that are common in fiber frequency comb design, must be evaluated more carefully than for other comb applications. The user must often try to minimize errors introduced by spectral fringing after the fact, once the damage is done in measurements.

Cepstral-domain analysis can help to evaluate the spectral baseline [64, 65] and ignore interferogram delays where parasitic copies dominate, thus more easily

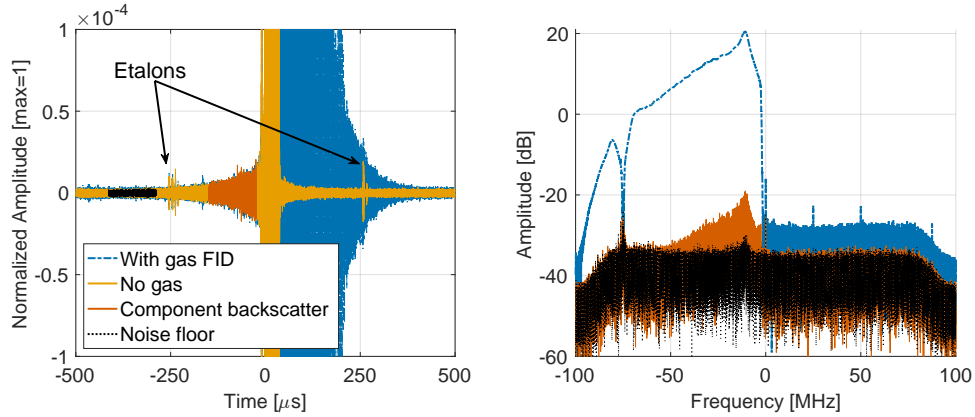


Figure 13. Parasitic reflections create time-delayed copies of the interferogram. When coupled with reflections, back-scatter from fiber-optic components yield undesired signal on a continuous range of delays. Left: Interferogram with (blue) and without (yellow) free induction decay from a gas. Parasitic peaks at $250 \mu\text{s}$ delay are seen on either side of the reference (yellow) interferogram. Back-scatter from a component (fiber coupler here) leaves signal (red) on a delay range corresponding to the component's length. Right: Spectrum obtained by Fourier-transform of the different colored regions from the left panel showing the additive noise level (black) and the back-scatter contribution (red) having the same spectral shape as the main signal (blue).

removing spectral fringing. This will however always remain a software patch and shall never be considered as a substitute for minimizing parasitic reflection in the setup. Best results are always obtained when working on all fronts: minimize error sources at the hardware level as much as possible and remove what is remaining using after the fact corrections.

Blanking points in the interferogram to minimize the impact of etalons amounts to applying a window and hence it can no longer be claimed that the measurements is instrument lineshape (ILS) free. The spectrum will be convolved with the spectrum of the window function. Great care must thus be applied in choosing this windowing function. With cepstral analysis, this window can be applied upon fitting with a model to only the spectral residuals, not the total estimated spectrum [66].

Similarly, part of the back-scattered light from fiber optical components is coupled in the forward direction by the parasitic discrete reflections. This gives rise to time-delayed copies of the signal, but now on a continuous delay range and

with apparently noisy amplitude. Figure 13 (left) shows in red that some signal seems to be present just before the interferogram center burst, where the impulse response should be zero. The right panel shows that a Fourier transform of this red section reveals a spectrum having the same shape as the main signal

In the case presented here, this is coming from surface roughness and inhomogeneity arising in the fused section during the fabrication of the fiber coupler. This is why this signal is seen over a limited interferogram delay range. For the measurement in [61], several couplers were characterized to minimize this contribution.

Back-scattering also occurs in the chirping fiber and if this fiber is longer than the comb's inter-pulse spacing, typically a few meters, signal can then show up everywhere in the interferogram. Figure 14 shows that in such cases Fourier transforming any small section of the interferogram away from the zero path difference reveals an apparently noisy signal again following the main signal spectral shape. When all other error sources are minimized, this currently yields a systematic error floor level of ~ 40 dB. A parasitic signal with a 0.01% spectral amplitude is added in an uncontrolled manner.

The noise-like feature of the back-scattered signal comes from the spatial randomness of the refraction index inhomogeneities. If the fiber in the setup is stable, the noisy back-scatter trace is repeatable. At first, it may seem that perturbing the fiber such as to change the speckle realization may provide a way to average out this contribution. This however transforms the constant noise-like signal to a source of time-varying excess noise that is very slow to average. The data in figure 13 for instance is an 85 minutes continuous average and is limited by the backscattering floor.

To the contrary, it has been confirmed that by regulating the optical fiber temperature such as to stabilise the fiber spatial inhomogeneities, an appreciable portion of the back-scatter signal is removed when ratioing with a reference measurement. This is in-line with the interpretation that back-scattering comes from a continuous random distribution of parasitic reflections and that stable etalons cancel out upon calibration.

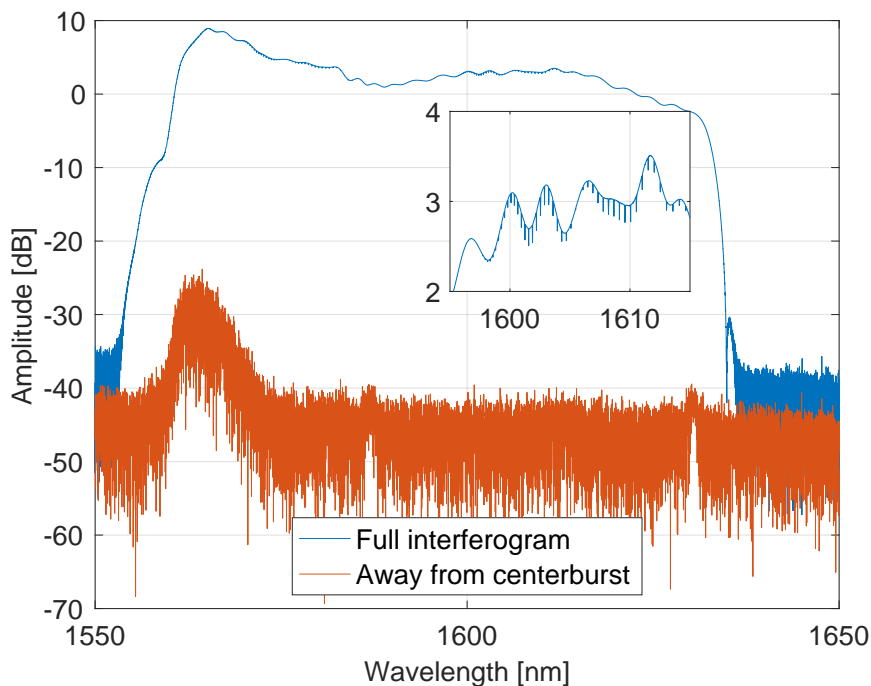


Figure 14. Back-scattering in optical fibers limits the systematic error noise floor of fiber-based DCS to 0.1%. A 85 minutes average is presented here.

5. Conclusion

Several sources of systematic errors in dual-comb interferometry have been identified and quantified. These include detection and acquisition chain non-linearity, self and cross phase modulation as well as incoherent spectral broadening. Parasitic reflections and back-scattering are also discussed.

For several instances, methods to identify and mitigate systematic errors are proposed. Table 1 list error sources, methods to observe and diagnose them as well as mitigation approaches. A visual design tool, the dynamic range diagram (fig. 8), is introduced to help optimize acquisition chains.

We argue here that since long-term real-time averaging is now available for DCS, practical measurements are often no longer limited by random noise, but by one or several systematic errors. This means that comparing DCS instruments using a figure

Systematic Errors	Diagnostic	Mitigation
Amplification chain/photo-detector NL	- Measure impulse response - FFT on IGM center burst for different input powers	- Add chirping element - Reduce amplifier gain - Increase photo-detector BW - Reduce input power
Acquisition card NL	- Measure INL of the ADC	- Add dither to the spectroscopy channel
Pulse interaction	- Measure absorption line asymmetry for different input powers and common fiber lengths	- Reduce input power to the common fiber - Reduce common fiber length - Add chirping element
Non-linear response of the sample	- Measure absorption line asymmetry for different pulse peak powers in the sample	- Reduce input power in the sample - Add chirping element - Increase beam size
Non-coherent spectral broadening	- Measure pulse to pulse phase/timing noise	- Change broadening method
Etalons	- Measure the impulse response of the dual-comb spectrometer	- Eliminate or minimize etalons - Calibrate with a reference spectrum
Back-scattering	- FFT away from the center burst of a high SNR IGM	- Reduce fiber length - Calibrate with a reference spectrum

Table 1. Systematic Errors, Diagnostics, hardware and software Mitigations

of merit (FOM) for the signal to noise ratio reached in 1 second is no longer providing a fair comparison basis. In practice, when averaging in real-time, the signal to noise ratio usually stops improving after a few minutes for laboratory measurements. Further improvements in measurement quality must rely on minimizing systematic errors.

‡ Disclaimer

Certain equipment or instruments are identified in this paper in order to specify the experimental procedure adequately. Such identification is not intended to imply recommendation or endorsement of any product by NIST, nor is it intended to imply that the equipment identified are necessarily the best available for the purpose.

References

- [1] Coddington I, Newbury N and Swann W 2016 *Optica*
- [2] Picqué N and Hänsch T W 2019 *Nature Photonics* **13** 146–157 ISSN 1749-4893
- [3] Rieker G B, Giorgetta F R, Swann W C, Kofler J, Zolot A M, Sinclair L C, Baumann E, Cromer C, Petron G, Sweeney C, Tans P P, Coddington I and Newbury N R 2014 *Optica* **1** 290–298
- [4] Karlovets E, Gordon I, Konnov D, Muraviev A and Vodopyanov K 2020 *Journal of Quantitative Spectroscopy and Radiative Transfer* **256** 107269 ISSN 0022-4073
- [5] Coburn S, Alden C B, Wright R, Cossel K, Baumann E, Truong G W, Giorgetta F, Sweeney C, Newbury N R, Prasad K, Coddington I and Rieker G B 2018 *Optica* **5** 320–327
- [6] Abbas M A, Dijk L v, Jahromi K E, Nematollahi M, Harren F J M and Khodabakhsh A 2020 *Sensors* **20** ISSN 1424-8220
- [7] Liu J, Huang B, Soskind M and Wysocki G 2023 Standoff hyperspectral imaging using a mid-IR quantum cascade laser dual-comb spectrometer *Quantum Sensing and Nano Electronics and Photonics XIX* vol PC12430 ed Razeghi M, Khodaparast G A and Vitiello M S International Society for Optics and Photonics (SPIE) p PC1243007
- [8] Lisak D, Charczun D, Nishiyama A, Voumard T, Wildi T, Kowzan G, Brasch V, Herr T, Fleisher A J, Hodges J T, Ciuryło R, Cygan A and Masłowski P 2022 *Scientific Reports* **12** 2377 ISSN 2045-2322
- [9] Roy J, Deschênes J D, Potvin S and Genest J 2012 *Opt. Express* **20** 21932–21939
- [10] Burghoff D, Yang Y and Hu Q 2016 *Science Advances* **2** e1601227
- [11] Hébert N B, Lancaster D G, Michaud-Belleau V, Chen G Y and Genest J 2018 *Opt. Lett.* **43** 1814–1817
- [12] Ycas G, Giorgetta F R, Baumann E, Coddington I, Herman D, Diddams S A and Newbury N R 2018 *Nature Photonics* **12** 202–208 ISSN 1749-4893
- [13] Sterczewski L A, Westberg J and Wysocki G 2019 *Opt. Express* **27** 23875–23893
- [14] Tian H, Li R, Sterczewski L A, Kato T, Asahara A and Minoshima K 2022 *Opt. Express* **30** 28427–28437
- [15] Walsh M, Kasic J, Cossel K C and Genest J 2024 *Review of Scientific Instruments* **95** 103005
- [16] Bell R J 1972 *Introductory Fourier Transform Spectroscopy* (New-York, NY, USA: Academic Press) ISBN 0 12-085150-4
- [17] Davis S, Abrams M and Brault J 2001 *Fourier Transform Spectrometry* (Academic Press)
- [18] Truong G W, Cossel K, Waxman E, Giorgetta F, Coddington I and Newbury N 2016 Phase

- noise-induced biases in coherent dual-comb spectroscopy *Conference on Lasers and Electro-Optics* (Optica Publishing Group) p SW1H.2
- [19] Hébert N B, Michaud-Belleau V, Deschênes J D and Genest J 2019 *IEEE Journal of Quantum Electronics* **55** 1–11
- [20] Coddington I, Swann W C and Newbury N R 2008 *Phys. Rev. Lett.* **100**(1) 013902
- [21] Rieker G 2023 Practical dual comb spectroscopy to improve energy systems: Navigating the interfaces between science, engineering and industry Plenary talk at the Optics and Photonics for Sensing the Environment Congress university of Colorado Boulder, USA
- [22] Ideguchi T, Poisson A, Guelachvili G, Picqué N and Hänsch T W 2014 *Nature Communications* **5** 3375
- [23] Boudreau S, Levasseur S, Perilla C, Roy S and Genest J 2013 *Opt. Express* **21** 7411–7418
- [24] Boudreau S and Genest J 2014 *Opt. Express* **22** 8101–8113
- [25] Teleanu E L, Durán V and Torres-Company V 2017 *Opt. Express* **25** 16427–16436
- [26] Zhu Z and Wu G 2018 *Engineering* **4** 772–778 ISSN 2095-8099
- [27] Taurand G, Giaccari P, Deschênes J D and Genest J 2010 *Appl. Opt.* **49** 4413–4419
- [28] Kang J, Feng P, Li B and Wong K K Y 2018 Dual-comb optical coherence tomography *Advanced Photonics 2018 (BGPP, IPR, NP, NOMA, Sensors, Networks, SPPCom, SOF)* (Optica Publishing Group) p SeTu3H.2
- [29] Xu L, Zhang L, Wang K, Liu C, Zhang C and Zhang X 2022 *Opt. Express* **30** 39014–39024
- [30] Ellis J L, Bodine M I, Swann W C, Stevenson S A, Caldwell E D, Sinclair L C, Newbury N R and Deschênes J D 2021 *Phys. Rev. Appl.* **15**(3) 034002
- [31] Chase D B 1984 *Applied Spectroscopy* **38** 491–494
- [32] Carter R O, Lindsay N E and Beduhn D 1990 *Applied Spectroscopy* **44** 1147–1151
- [33] Lachance R L 2000 Non-linearity correction of FTIR instruments *Fifth Workshop of Infrared Emission Measurements by FTIR* (Quebec)
- [34] Waxman E M, Cossel K C, Truong G W, Giorgetta F R, Swann W C, Coburn S, Wright R J, Rieker G B, Coddington I and Newbury N R 2017 *Atmospheric Measurement Techniques* **10** 3295–3311
- [35] Guelachvili G 1986 *Applied Optics* **25** 4644–4648
- [36] Texas Instruments 2018 *OPA847: Ultra-Low-Noise, High-Speed, Voltage-Feedback Operational Amplifier* <https://www.ti.com/lit/ds/symlink/opa847.pdf>
- [37] Diddams S A, Kirchner M, Fortier T, Braje D, Weiner A M and Hollberg L 2009 *Opt. Express* **17** 3331–3340
- [38] Williams K, Esman R and Dagenais M 1994 *IEEE Photonics Technology Letters* **6** 639–641
- [39] Guay P, Walsh M, Tourigny-Plante A and Genest J 2023 *Opt. Express* **31** 4393–4404
- [40] Guay P, Tourigny-Plante A, Michaud-Belleau V, Hébert N B, Gouin A and Genest J 2021 *OSA Continuum* **4** 2460–2467
- [41] Malarich N A, Cossel K C, Deschenes J D, Giorgetta F R, Washburn B R, Newbury N R, Genest J and Coddington I 2023 *Opt. Express* **31** 29074–29084
- [42] Corporation A 2007 6022B–CASIC–20-Dec-07 Tech. rep. Atmel Corporation available at Atmel website
- [43] Devices A 1994 Overcoming converter nonlinearities with dither, AN-410: APPLICATION

- NOTE Tech. rep. Analog Devices One Technology Way, P.O. Box 9106, Norwood, Massachusetts 02062-9106 available at Analog Devices website
- [44] Melkonian L 1992 Improving A/D Converter Performance Using Dither, Application Note 804 Tech. rep. National Semiconductor 2900 Semiconductor Drive, Santa Clara, California 95051 available at Texas Instruments website
- [45] e2v semiconductor sas 2007 Application Note 0869B-BDC-06/07 Tech. rep. e2v semiconductor sas available at e2v semiconductor website
- [46] Kauppinen J, Salomaa I and Ahro M 2001 Compression of the interferogram by chirping *First International Conference on Advanced Vibrational Spectroscopy (ICAVS-1)* (Turku, Finland) paper D2
- [47] Desbiens R, Tremblay P, Farley V, Legault J F and Chamberland M 2003 Field widening effects on modulation efficiency and ILS resulting from the use of uncompensated beam splitter *11th International Workshop on Atmospheric Science from Space Using Fourier Transform Spectrometry* (Bad Wildbad, Allemagne)
- [48] Mertz L 1967 *Journal of the Optical Society of America* **57** iv
- [49] Deschênes J D, Giaccari P and Genest J 2010 *Opt. Express* **18** 23358–23370
- [50] Guay P, Walsh M and Genest J 2022 *Opt. Lett.* **47** 4275–4278
- [51] Walsh M, Baumann E, Malarich N, Egbert S, Cole R K, Rieker G B, Newbury N R, Coddington I, Cossel K and Genest J 2024 *Opt. Express* **32** 19837–19853
- [52] Béjot P and Kasparian J 2018 *Phys. Rev. A* **97**(6) 063835
- [53] Mitschke F M and Mollenauer L F 1987 *Opt. Lett.* **12** 355–357
- [54] Olivier M and Piché M 2009 *Opt. Express* **17** 405–418
- [55] Brault J W 1985 Fourier transform spectrometry *High Resolution in Astronomy* ed Benz A O, Huber M C E and Mayor M (Saas-Fee: Swiss Society of Astronomy and Astrophysics) pp 1–61 proceedings of the 15th Advanced Course of the Swiss Society of Astronomy and Astrophysics
- [56] Ott C, Kaldun A, Raith P, Meyer K, Laux M, Evers J, Keitel C H, Greene C H and Pfeifer T 2013 *Science* **340** 716–720
- [57] Schippers S 2018 *Journal of Quantitative Spectroscopy and Radiative Transfer* **219** 33–36
- [58] Fano U 1961 *Physical Review* **124** 1866–1878 received July 14, 1961
- [59] Riffe D M 2011 *Phys. Rev. B* **84**(6) 064308
- [60] Rosenkranz P 1975 *IEEE Transactions on Antennas and Propagation* **23** 498–506
- [61] Walsh M, Genest J, Cossel K C and Fleisher A J 2024 Carbon dioxide band intensity ratio measurement by dual comb spectroscopy *The 17th International HITRAN Conference (combined with the 16th ASA Conference)*
- [62] Neely T W, Johnson T A and Diddams S A 2011 *Optics Letters* **36** 4020–4022
- [63] Gambetta A, Coluccelli N, Cassinero M, Gatti D, Laporta P, Galzerano G and Marangoni M 2013 *Optics Letters* **38** 1155–1157
- [64] Cole R K, Makowiecki A S, Hoghooghi N and Rieker G B 2019 *Optics Express* **27** 37920–37939
- [65] Goldenstein C S, Mathews G C, Cole R K, Makowiecki A S and Rieker G B 2020 *Applied Optics* **59** 7865–7875
- [66] Walsh M, Malarich N, Giorgetta F R, Coddington I and Genest J 2023 Reconciling cepstral

and spectral spectroscopic fits *Optica Sensing Congress 2023 (AIS, FTS, HISE, Sensors, ES)* (Optica Publishing Group) p JM2B.3